

# ADVANCED MATERIALS

## Supporting Information

for *Adv. Mater.*, DOI: 10.1002/adma.201702184

Polymer:Fullerene Bimolecular Crystals for Near-Infrared  
Spectroscopic Photodetectors

*Zheng Tang,\* Zaifei Ma, Antonio Sánchez-Díaz, Sascha  
Ullbrich, Yuan Liu, Bernhard Siegmund, Andreas Mischok,  
Karl Leo, Mariano Campoy-Quiles, Weiwei Li,\* and Koen  
Vandewal\**

## Supporting Information

**Polymer:Fullerene Bimolecular Crystals for Near-Infrared Spectroscopic Photodetectors**

*Zheng Tang\*, Zaifei Ma, Antonio Sánchez-Díaz, Sascha Ullbrich, Yuan Liu, Bernhard Siegmund, Andreas Mischok, Karl Leo, Mariano Campoy-Quiles, Weiwei Li\*, and Koen Vandewal\**

## Table of Contents

SI-1. Methods .....	2
SI-2. Derivation of analytic formulas .....	4
SI-3. Studies on photodetectors based on P3HT and PCBM .....	7
SI-4. Studies on photodetectors based on PDPPTDTPPT:SdiCNPBI .....	9
Figure S5. Determination of the CT state energy in the PBTTT:PCBM and P3HT:PCBM blends .....	11
Figure S6. Influence of surface roughness on EQE .....	11
Figure S7. Effect of an additional PBTTT layer .....	11
Figure S8. Parasitic electrode absorption losses .....	12
Figure S9. Reflectance of DBRs .....	12
Figure S10. JV characteristics of DBR based photodetectors .....	13
Figure S11. Spectral response of photodetecting pixels in a miniaturized spectrometer .....	13
Table S1. Performance parameters for metal-metal detectors .....	14
Table S2. Performance parameters for DBR detectors .....	14
References .....	14

## SI-1. Methods

**Materials and Devices:** PEIE and P3HT were purchased from Sigma-Aldrich, PBTTT(c14) was purchased from Solarmer Energy, Inc. and PCBM was purchased from Lumitec. PDPPTDTPT and SdiCNPBI were synthesized according to references.<sup>1,2</sup>

The metal-metal cavity detectors were constructed on top of pre-cleaned glass. A semi-transparent Au mirror was deposited on glass via thermal evaporation through a shadow mask under a vacuum pressure of less than  $10^{-7}$  mbar, at a rate of  $1 \text{ Å s}^{-1}$ . The thickness of the Au layer was 30 nm. The Au mirror was modified by a spin-coated PEIE layer to act as the cathode of the detector. PEIE solution was diluted by a factor of 2000 in isopropanol, and the spin-coating speed was 2000 rpm. To reduce the surface roughness of the active layer and improve the morphology of the BHJ blend, mixed solvents of chloroform and orthodichlorobenzene (oDCB) were used for the active inks. For the system based on PBTTT:PCBM (donor:acceptor: 1:4, weight ratio), the chloroform:oDCB mixing volume ratio was 6:4. For the system based on P3HT:PCBM and PDPPTDTPT: SdiCNPBI, the chloroform:oDCB ratio was 8:2. To achieve first order resonance wavelengths, a total concentration of 8-15  $\text{mg ml}^{-1}$  was used for the solution, and to achieve second order resonances, the concentration was 30-35  $\text{mg ml}^{-1}$ . The active layer was deposited on top of the PEIE modified Au mirror via three-step spin-coating. The first step was 400 rpm for 25 s, and the ink was deposited while the spinner was running. The second step (30 s) was varied between 500-1500 rpm for controlling the thickness of the active layer. The last step was 2000 rpm (5 s) for removing the residual solution. The active layer was still wet after spin coating, and it was then left in a nitrogen filled glovebox for about 8 hours to dry. After that, a 10 nm thick  $\text{MoO}_3$  layer followed by a 100 nm thick Ag layer were subsequently evaporated on top of the dry active layer under a pressure of less than  $10^{-6}$  mbar. The evaporation rates were 0.1 and  $2 \text{ Å s}^{-1}$  for  $\text{MoO}_3$  and Ag, respectively. The active area (0.01 to  $0.05 \text{ cm}^2$ ) of the device is determined by the overlapping area between the bottom and the top metal electrodes.

DBRs were fabricated on clean glass substrates, with  $\text{TiO}_2$  and  $\text{SiO}_2$  layers alternatively deposited with an e-beam evaporator under a base pressure of  $\sim 10^{-6}$  mbar and a partial oxygen pressure of  $\sim 10^{-4}$  mbar to prevent the formation of Ti suboxides. A total of 21 layers, with the last layer being a  $\text{TiO}_2$  layer, were used to achieve a reflectance over 99.9% in the stopband of the DBR. The thickness of the  $\text{TiO}_2$  layers and the  $\text{SiO}_2$  layers were 90 nm and 130 nm, respectively, resulting in a reflecting stopband centered around 750 nm. For a stopband around 850 nm, the thickness of the  $\text{TiO}_2$  and  $\text{SiO}_2$  layers were 100 nm and 145 nm, respectively. For constructing a DBR based cavity detector, a 20 nm thick PEDOT:PH1000 layer was deposited on top of the DBR by spin coating. The PEDOT PH1000 solution was purchased from Heraeus, and diluted with deionized water at a 1:1 ratio. Ethylene glycol (6%, vol%), the surfactant Zonyl FS-30 (0.5%, vol%), and silquest A-187 (0.025%, vol%) were added into the diluted PEDOT solution to increase conductivity, surface smoothness and layer adhesion of the PEDOT layer. A spin coating speed of 3000 rpm was used for depositing the PEDOT layer. The PEDOT coated DBR was further modified by a thin PEIE layer. The rest of the procedures used for constructing the DBR based devices were the same as those for a metal-metal cavity device, except that the top Ag mirror for the DBR detectors was 30 nm thick.

Miniature spectrometers were constructed on top of pre-cleaned standard microscope glass slides. Deposition of Au and  $\text{MoO}_3/\text{Ag}$  electrodes was carried out following the same settings as for metal-metal cavity photodetectors. PEIE was deposited at an elevated temperature ( $50^\circ\text{C}$ ), using a blade coater with a constant coating speed ( $10 \text{ mm s}^{-1}$ ). The gap distance between blade and substrate was 150  $\mu\text{m}$ . The PEIE solution was diluted by a factor of 1000 in isopropanol. The active ink based on PBTTT:PCBM (1:4) was prepared using mixed solvents (chlorobenzene:oDCB, 1:1 ratio) with a total concentration of 40  $\text{mg ml}^{-1}$ . Active solution was stirred and heated at  $80^\circ\text{C}$  for about 12 hours, prior to use. Deposition of the active layer was done in a nitrogen filled glove box, using a blade coater with a decreasing coating speed. The initial speed was  $38 \text{ mm s}^{-1}$ , and it was gradually decreased to  $13 \text{ mm s}^{-1}$ , within a coating distance of 6 cm. Coating was carried out at a temperature of  $110^\circ\text{C}$ , at a gap distance of 150  $\mu\text{m}$ . After device fabrication, a PBTTT layer, acting as a cut-off filter, for eliminating above gap excitation was prepared on a separate glass slide through drop casting.

**Characterization:** EQE spectra were measured using a monochromator and a chopped and collimated halogen lamp light source. In addition to the order sorting filters, a lowpass filter was used for wavelengths longer than 1100 nm to eliminate the second harmonics from the light source. The chopping frequency was 173 Hz. The photo response signals from the cavity detectors were amplified by a pre-amplifier and recorded by a lock-in amplifier. The photon flux from the monochromator was calibrated with a Si and an InGaAs diode. For devices based on DBRs, the NIR part of the EQE spectrum was measured with Fourier Transform Photocurrent Spectroscopy (FTPS)<sup>3,4</sup> for a sub-nanometer resolution, and the measured FTPS-EQE was attached to the above gap EQE measured with the monochromator containing EQE setup. This procedure ensures that the measured FWHM was not affected by the spectral resolution of the monochromator system used, as FTPS has a much better spectral resolution.

Current-voltage characteristic curves were measured with a Keithley 2400 SourceMeter. The thickness of the active layer was measured with a Dektak surface profilometer.

Estimations of above gap absorption coefficients of the BHJ systems were determined using Beer-Lambert's law for films coated on glass substrates. Three films with different thicknesses were used for each materials system. Transmission and reflection were measured using a Lambda 850 spectrometer. The spectral shape of CT absorption coefficients was determined using the formula described in reference.<sup>4</sup> The spectra were normalized to the above gap absorption coefficients for accurate determination the CT absorption coefficients. For TM simulations, the dielectric functions of the interlayers and the electrodes were obtained by modeling the transmission and reflection of thin films deposited on glass substrates. Atomic force microscopy images were taken with an AIST-NT combiscope 1000 using tapping mode.

The transient photocurrent response was measured with a ND-YAG laser (PL2210 Ekspla) with a pulse length of 25 ps and an excitation wavelength of 1064 nm. Signals were recorded with an oscilloscope DPO7354C, Tektronix.

The linear dynamic range was measured using neutral density filters, and the EQE setup for irradiances lower than 1 mW cm<sup>-2</sup>. For irradiance higher than 1 mW cm<sup>-2</sup> the photocurrent response was measured with an LED and a Keithley 2400 SourceMeter.

Spectral response of the miniaturized spectrometers was measured with a supercontinuum LASER model SC400 from NKT photonics, a monochromator model LLTF Contrast also from NKTPhotonics and a power meter PM100D with a sensor S120VC, all controlled with a homemade Labview software . A PBTTF filter was placed in front of all the pixels and an additional low pass filter with a cut-off wavelength at 850 nm was employed for the pixels with response above 850nm. The photocurrent was monitored with a Keithley SourceMeter model 2450-EC. The water transmittance was measured using a light source (Solar Simulator (SAN-EI Electric, XES-100S1)) and measuring the photocurrent with a Keithley SourceMeter model 2450-EC. The transmittance spectrum was determined by taken the ratio between the photocurrents measured with and without water in between the light source and the spectrometer for every pixel, and plotted for its corresponding wavelength, i.e, the wavelength at which the maximum photodetector spectral response was achieved. (The incoming light is perpendicular to the sample (water) and the detector (the spectrometer) plane, and the illumination area is about 10 cm<sup>2</sup> x 10 cm<sup>2</sup>, much larger than the area of the spectrometer.)

**Calculation of specific detectivity:** we used the following equation to calculate specific detectivity

$$D^* = \frac{\lambda \cdot EQE}{hc \cdot i_{noise}} \text{ in unit of Jones,}$$

where  $h$  is the Planck's constant and  $c$  is speed of light. The noise current  $i_{noise}$  is calculated via

$$i_{noise} = \sqrt{2qi_d + \frac{4kT}{R_{sh}}} ,$$

where  $q$  is elementary charge,  $i_d$  is the dark current density,  $R_{sh}$  is the shunt resistance,  $k$  is the Boltzmann constant, and  $T$  is absolute temperature. We calculated  $D^*$  for a short-circuit condition, at which  $2qi_d = 0$ .

## SI-2. Derivation of analytic formulas

In a simplified model related to the cavity device architecture proposed by Kishino et al.<sup>5</sup>, the photo-absorbing active layer is sandwiched in between two mirrors, which also simultaneously act as the electrodes (Scheme S1). Assuming that the interfaces between the mirrors and the active layer are responsible for the absorption losses in the mirrors/electrodes, we can derive that the absorption ( $A$ ) in the active layer of the cavity device depends on the wavelength  $\lambda$ , through

$$A = \frac{(e^{-\tau_1} + e^{-\tau_2} R_2 e^{-aL})}{1 - 2\sqrt{R_1 R_2} e^{-aL} \cos(x) + R_1 R_2 e^{-2aL}} A_0 \quad (1)$$

where

$$x = \frac{4\pi L n}{\lambda} \quad (2)$$

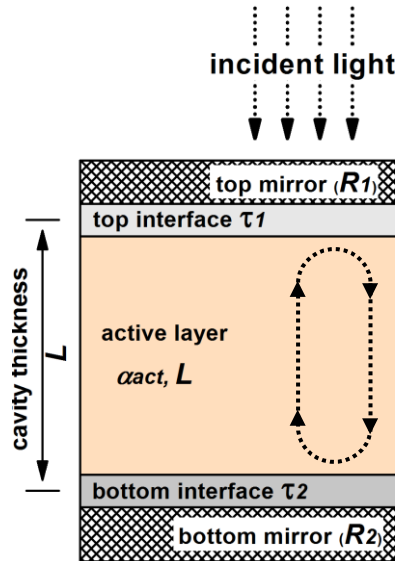
$L$  is the thickness of the media between the two mirrors, which is the thickness of the active layer in the simplified model.  $n$  is the effective refractive index of the media in between two mirrors,  $R_1$  and  $R_2$  are the reflectance of the top and bottom mirrors,  $\tau_1$  and  $\tau_2$  are the optical depths of the mirrors, and  $a$  is the effective absorption coefficient

$$\alpha = \frac{\tau_1 + \alpha_{act} L + \tau_2}{L} \quad (3)$$

additionally

$$A_0 = (1 - R_1)(1 - e^{-a_{act} L}) \quad (4)$$

which is the approximate fraction of absorbed light upon a single pass through a non-enhanced active layer.



**Scheme S1.** A schematic picture of a simple cavity detector with both the bottom and the top mirrors acting simultaneously as mirrors and the electrodes.

A constructive interference condition is achieved when

$$\cos(x) = 1$$

This leads to a dependence of resonance wavelengths on the cavity thickness and refractive index

$$\lambda_m = \frac{2nL}{m} \quad (5),$$

where  $m$  is a natural number  $> 0$  representing the order of the resonance.

$A$  reaches a maximum  $A_{max}$  at the resonance wavelength  $\lambda_m$

$$A_{max} = A(\lambda_m) = \frac{(e^{-\tau_1} + e^{-\tau_2} R_2 e^{-aL})}{(1 - \sqrt{R_1 R_2} e^{-aL})^2} A_0 \quad (6),$$

and  $A_{max}$  reaches its highest possible value when

$$R_2 = 1 \text{ and } e^{-aL} = \sqrt{R_1}.$$

To derive the FWHM ( $\Delta\lambda$ ), we first use equation (1) and (6) to determine  $x$  at  $\frac{1}{2} A_{max}$

$$\begin{aligned} \frac{1}{2} A_{max} &= \frac{(e^{-\tau_1} + e^{-\tau_2} R_2 e^{-aL}) A_0}{2(1 - \sqrt{R_1 R_2} e^{-aL})^2} = \frac{(e^{-\tau_1} + e^{-\tau_2} R_2 e^{-aL}) A_0}{1 - 2\sqrt{R_1 R_2} e^{-aL} \cos(x) + R_1 R_2 e^{-2aL}} \\ \Rightarrow \cos(x) &= 2 - \frac{1 + R_1 R_2 e^{-2aL}}{2\sqrt{R_1 R_2} e^{-aL}}. \end{aligned}$$

Taylor expansion gives

$$\cos(x) \approx 1 - \frac{x^2}{2},$$

therefore

$$x = \frac{1 - \sqrt{R_1 R_2} e^{-aL}}{\sqrt{\sqrt{R_1 R_2} e^{-aL}}},$$

and the FWHM value in  $x$ -space ( $\Delta x$ ) is thus

$$\Delta x = 2x = \frac{2 - 2\sqrt{R_1 R_2} e^{-aL}}{\sqrt{\sqrt{R_1 R_2} e^{-aL}}} \quad (7).$$

From equation (2), we have

$$dx = -\frac{4\pi L n}{\lambda} \left( \frac{d\lambda}{\lambda} \right) \Rightarrow \frac{dx}{x} = \frac{d\lambda}{\lambda},$$

Hence

$$\frac{\Delta x}{x} = \frac{\Delta \lambda}{\lambda} \quad (8).$$

Combine equation (7) and equation (8) for the peak positions in  $\lambda$ -space and  $x$ -space, i.e.,  $\lambda = \lambda_m$ ,  $x = 2m\pi$ , we obtain

$$\begin{aligned} \frac{\Delta \lambda}{\lambda_m} &= \frac{1 - \sqrt{R_1 R_2} e^{-aL}}{m\pi \sqrt{\sqrt{R_1 R_2} e^{-aL}}} \\ \Rightarrow \Delta \lambda &= \lambda_m \frac{1 - \sqrt{R_1 R_2} e^{-aL}}{m\pi \sqrt{\sqrt{R_1 R_2} e^{-aL}}} \quad (9), \end{aligned}$$

with the mirror reflectances optimized for maximum EQE, i.e.,  $R_2 = 1$  and  $e^{-aL} = \sqrt{R_1}$ , equation (9) can be simplified to

$$\Delta \lambda \approx \lambda_m \frac{2aL}{m\pi} = \frac{a\lambda_m^2}{n\pi} \quad (10),$$

from which, it is clear that a lower absorption coefficient gives rise to a better spectral selectivity. From equation (10), we can also derive the upper boundary for the absorption coefficient of the active layer for a certain desired  $\Delta\lambda$ .

When the active layer absorption coefficient is low, parasitic absorption losses ( $\tau_1, \tau_2$ ) limit the

$EQE_{max}(\lambda_m)$ . This impose a lower limit for the absorption coefficient of the active layer. Using equation (6), and assuming 100% internal quantum efficiency and the same parasitic absorption losses at both mirrors, i.e,  $\tau_1 = \tau_2$ , we have

$$EQE_{max}(\lambda_m) = \frac{e^{-\tau}(1+R_2e^{-aL})}{(1-\sqrt{R_1R_2}e^{-aL})^2} A_0 \quad (11),$$

Where

$$\tau = \tau_1 = \tau_2 \quad ,$$

Using optimized mirror reflectances, i.e.  $R_2 = 1$  and  $e^{-aL} = \sqrt{R_1}$ , to combine equation (4) and equation (11), we derive

$$EQE_{max}(\lambda_m) = \frac{e^{-\tau}(1-e^{-a_{act}L})}{1-e^{-aL}} \quad ,$$

Taylor expansion gives

$$EQE_{max}(\lambda_m) = \frac{a_{act}}{a} \quad ,$$

and using equation (3), we have

$$\Rightarrow EQE_{max}(\lambda_m) \approx \frac{a_{act}}{a_{act} + \frac{2\tau}{L}} \quad (12).$$

Here does  $\frac{2\tau}{L}$  represent an effective absorption coefficient ( $a_{mirror}$ ) for the mirrors for an empty cavity with a cavity length of  $L$ , and it can be calculated from the FWHM of the absorption spectra of the empty cavity, using equation (10). For an empty cavity with a metal-metal structure, the FWHM is about 20 nm at first order resonances, according to TM simulations. Therefore,  $a_{mirror}$  depends on wavelength and it is approximately  $10^{-3}$  to  $10^{-4} \text{ nm}^{-1}$ . This allows us to calculate the absorption coefficient of the active materials system required to achieve a certain  $EQE_{max}$ , using equation (12).

Advantages of higher order resonances are implied by the derived analytical equations: According to equation (12), higher order resonances lead to higher EQE, due to a larger  $L$  that reduces the parasitic absorption losses in the mirrors. Equation (3) predicts that at a higher order resonance, the effective absorption coefficient is reduced, leading to a narrower spectral FWHM. It should be noted that the analytic formulas ignore the standing wave effects, and will therefore, lightly overestimate losses due to parasitic absorption.

### SI-3. Studies on photodetectors based on P3HT and PCBM

Analytical equation predicts an inferior spectral tunability for the metal-metal cavity detectors based on P3HT, compared to PBTTT, due to the lower absorption coefficient of the CT band in the P3HT:PCBM system. Experimentally, we also observe more significant losses due to a too rough surface of the active layer. The high surface roughness, seen in atomic force microscope (Figure S1), is related to the growth of P3HT crystals<sup>6</sup>, which is required for high electrical performance in photovoltaic devices based on P3HT.

The crystal growth of P3HT in the BHJ active layer can be suppressed by a faster drying during the film deposition, which gives smoother active layer (Figure S1) for a better wavelength selectivity (Figure S2a). However, this also leads to more pronounced recombination losses limiting IQE of the device. As a result, the EQE of the cavity detectors based on P3HT:PCBM (Figure S2b and S2c) is significantly lower than that of the detectors based on PBTTT.

The results emphasize the importance of processability, miscibility, as well as the dynamics during film formation of the active material systems for constructing the optical cavity devices using BHJ systems, and it suggests the need of these additional considerations while designing new materials.

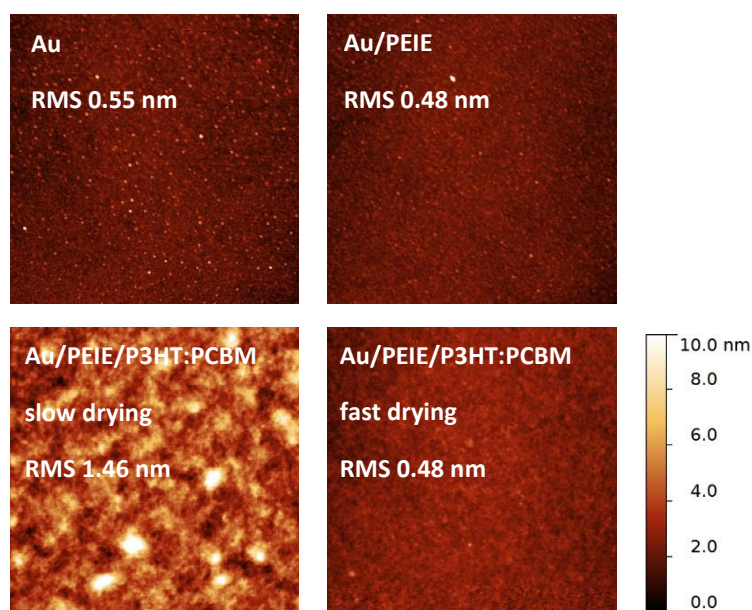


**Figure S1.** Atomic force microscopy images (5  $\mu\text{m} \times 5 \mu\text{m}$ ) of the surfaces of different layers in metal-metal cavity detectors. Note that the surface roughness values are only for the measured area. Macroscopic thickness variation of the active layer are believed to contribute additionally to the reduction of peak EQE and increase of spectral line width of the cavity devices.



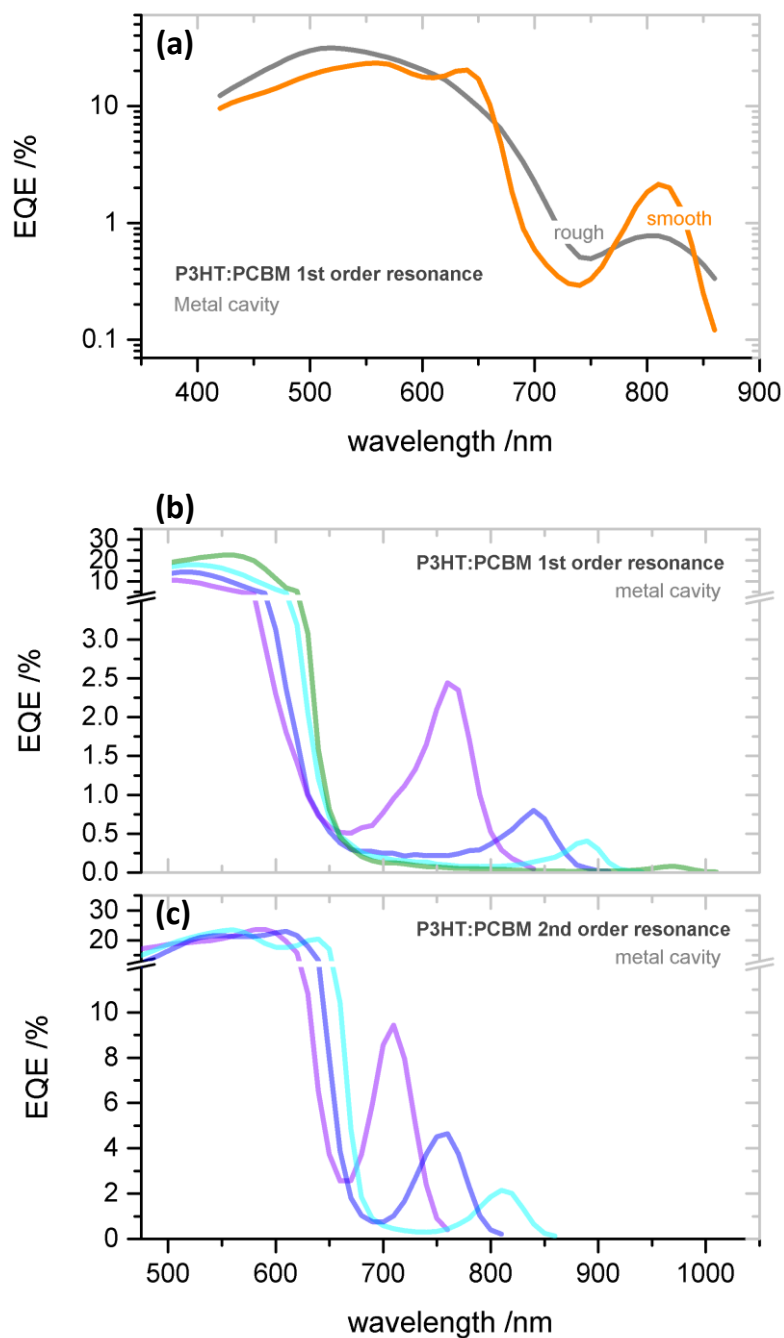


**Figure S2. a:** First order resonance EQE of metal-metal cavity detectors based on P3HT:PCBM. The spin-coating speeds for the rough and smooth active layer are 500 rpm and 3000 rpm, respectively. Different solution concentrations are used to achieve the same active layer thickness. **b:** First order resonance and **c:** second order resonance EQEs of metal-metal cavity detectors based on P3HT:PCBM with different active layer thicknesses.

## SI-4. Studies on photodetectors based on PDPPTDTPT:SdiCNPBI

To extend the detection wavelength of a cavity photodetector, we employed the system based on PDPPTDTPT: SdiCNPBI in a metal-metal cavity structure with first order resonances. The use of SdiCNPBI with a very low LUMO level (-4.5 eV) allows us to achieve  $E_{CT} \approx 0.7$  eV (Figure S3), suited for detecting wavelengths up to 1700 nm. With no effort towards optimization on the molecular or the device level, we obtain a lower EQE (Figure S4a), compared to PBTBT based systems. This is partially due to high parasitic absorption losses related to a too strong phase separation between the donor and the acceptor material, leading to weak CT absorption, since the blend of PDPPTDTPT and SdiCNPBI is most likely a non-intercalating system due to the size of the molecules.

Nevertheless, we show that the dark current of these devices is already fully minimized with no shunt current found in the diode characteristic curve (Figure S4d). In fact, due to the low energy of CT state, the diode characteristics do not depend on the active layer thickness, and the  $JV$  curve can be fitted with the diode equation with infinite shunt resistance. Consequently, a specific detectivity in the range of  $10^{10} - 10^8$  Jones is realized for these detectors operating in the wavelength range of 1100 - 1700 nm. Again, the optical cavity devices provide a remarkable selectivity and continuous spectral tunability (Figure S4b and Figure S4c).<sup>7</sup>

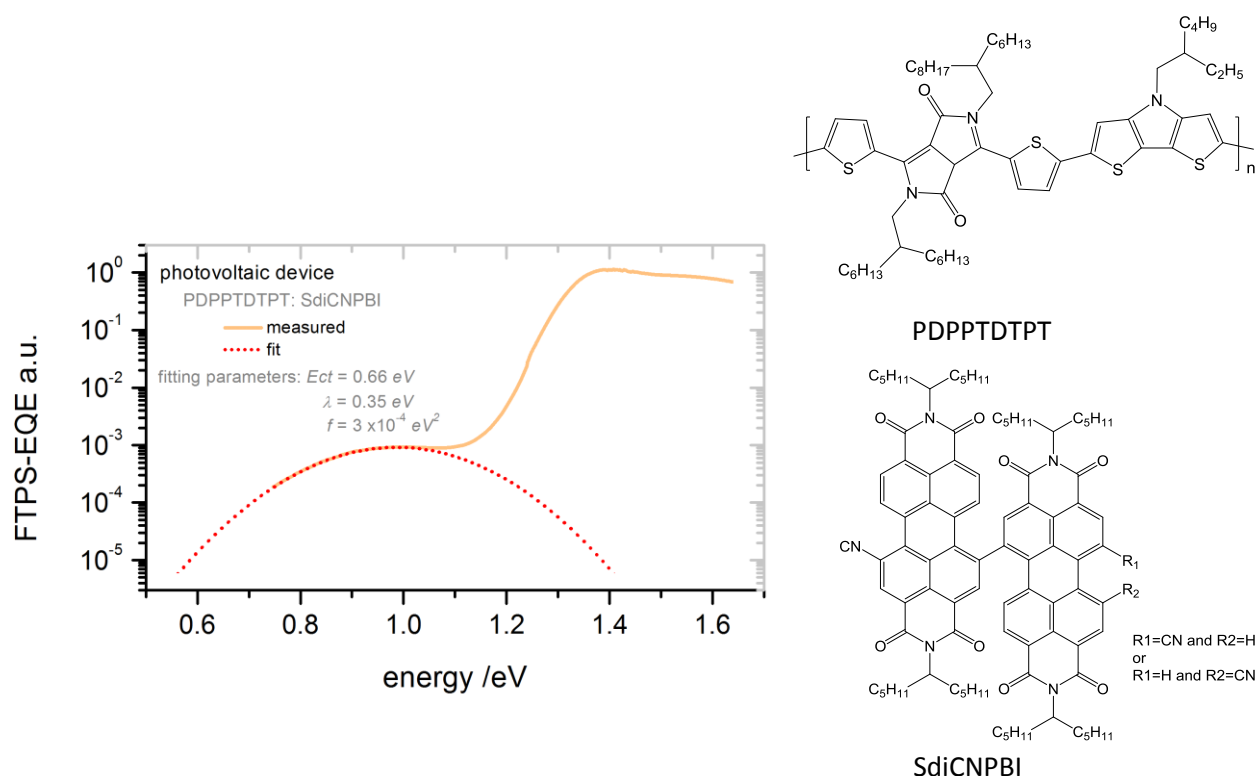


**Figure S3.** Determination of the CT state energy of PDPPTDTPT: SdiCNPBI using the FTPS method proposed in reference.<sup>8</sup> The architecture of the device constructed for the FTPS measurement is Glass/Au/PEIE/active layer/PEDOT:PSS PH1000. The morphology of the active layer of this device is expected to be identical to that of the cavity detectors, since the layers below the active layer in both devices are exactly the same.

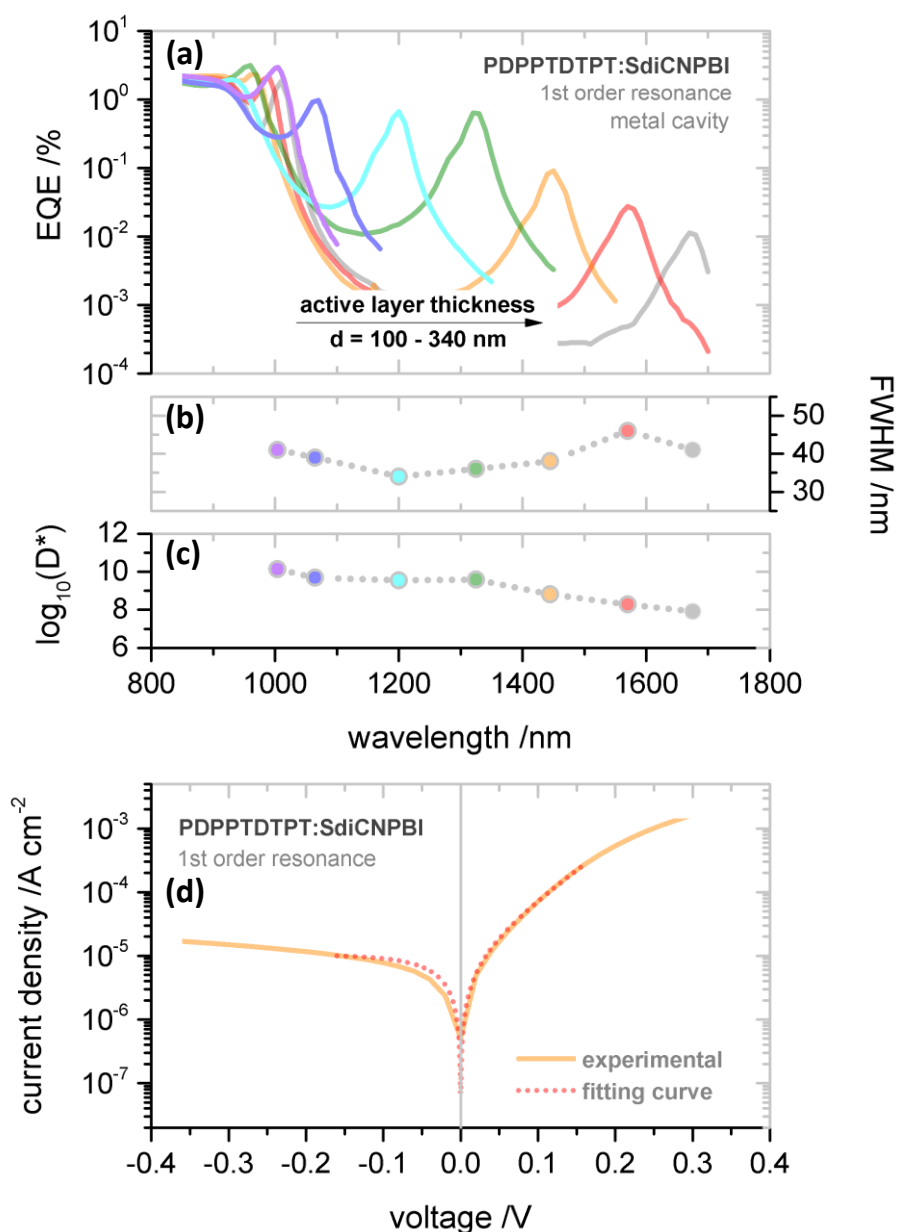


**Figure S4.** Performance of metal-metal cavity photodetectors based on PDPPTDTPT: SdiCNPBI (1:1). **a:** EQE, **b:** FWHM, and **c:** specific detectivity  $D^*$  (Jones) of devices with the active layer thickness varies between 100 - 340 nm for the first order resonance. **d:** dark  $JV$  characteristic curve fitted by an exponential diode equation  $J = J_0 \exp(qV/\eta kT)$  with infinitely high shunt resistance, where  $J_0$  ( $= 10^{-5} \text{ A cm}^{-2}$ ) is the saturation current,  $q$  is the elementary charge,  $\eta$  ( $= 2$ ) is the diode ideality factor,  $k$  is the boltzmann constant, and  $T$  is the temperature.

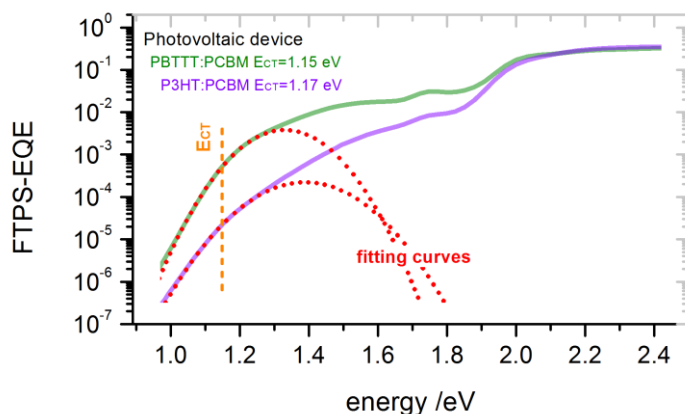


Figure S5. Determination of the CT state energy in the PBTTT:PCBM and P3HT:PCBM blends, using the FTPS method proposed in reference.<sup>8</sup>

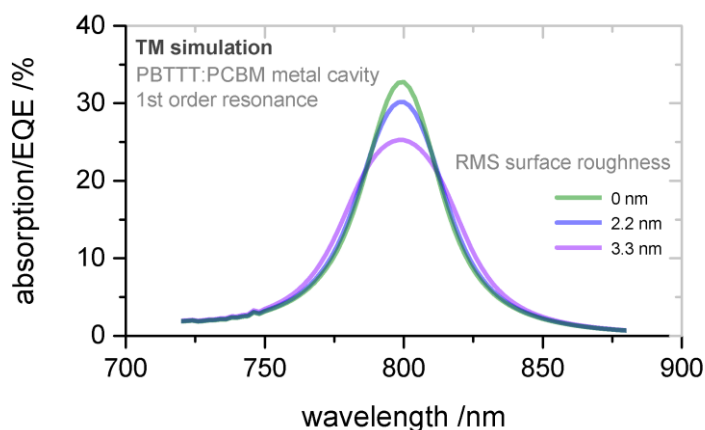


Figure S6. Influence of surface roughness on EQE of a metal-metal cavity detector based on PBTTT:PCBM simulated by a TM model.

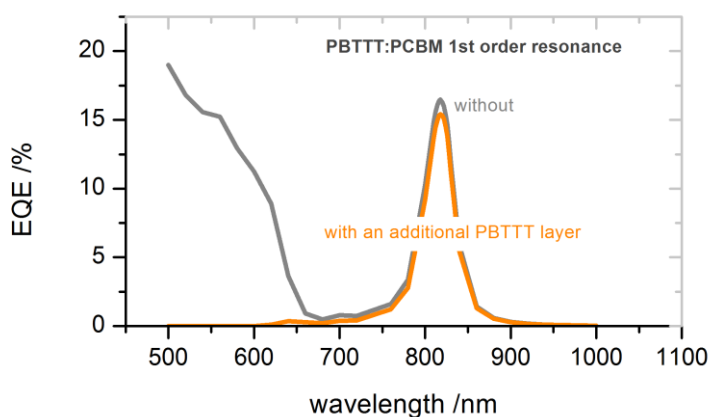
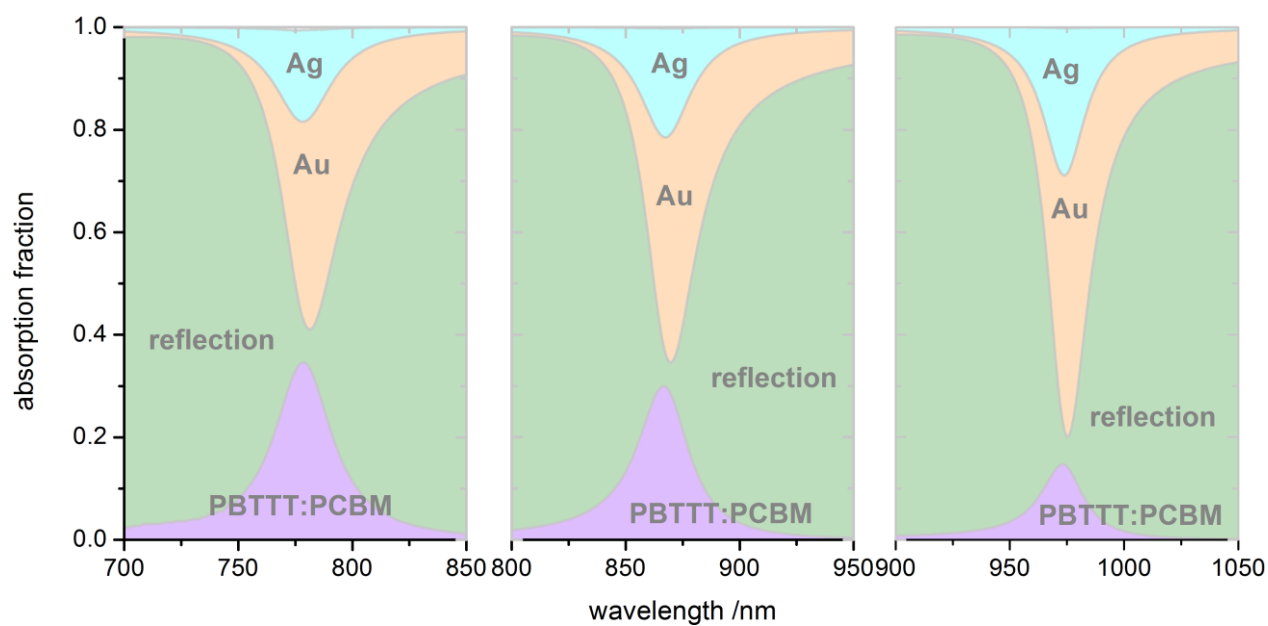
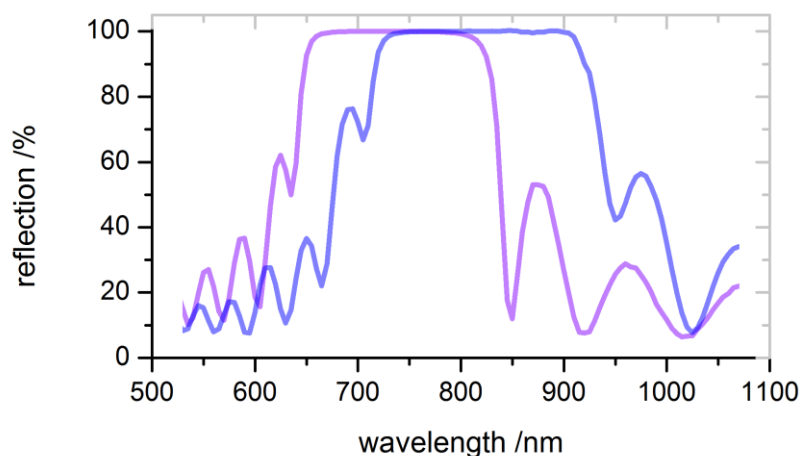


Figure S7. Effect of an additional PBTTT layer on top of Au for a metal-metal cavity detector based on PBTTT:PCBM. The additional PBTTT layer acts as a filter for wavelengths shorter than 650 nm, and thus suppresses the above gap absorption.



**Figure S8. Parasitic electrode absorption losses, reflection losses, and absorption in the active layer of a metal-metal cavity detector based on PBTTT:PCBM, simulated with a TM model for three different resonance wavelengths (first order resonance).**



**Figure S9.** Reflectance of DBRs based on alternating  $\text{TiO}_2$  and  $\text{SiO}_2$  layers. For the DBR with a reflection band centered at 750 nm, the thickness of  $\text{TiO}_2$  layers is 90 nm, and the thickness of  $\text{SiO}_2$  layers is 120 nm; for the DBR with a reflection band centered around 850 nm, the thickness of  $\text{TiO}_2$  layer is 100 nm, and the thickness of  $\text{SiO}_2$  layer is 140 nm. 21 layers are used in the DBRs with  $\text{TiO}_2$  being the top layer.

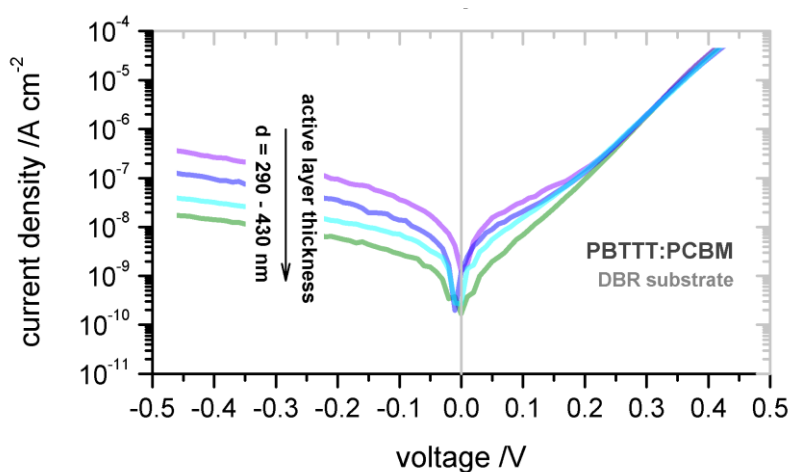


**Figure S10.** *JV* characteristics of DBR based photodetectors with different active layer thicknesses.

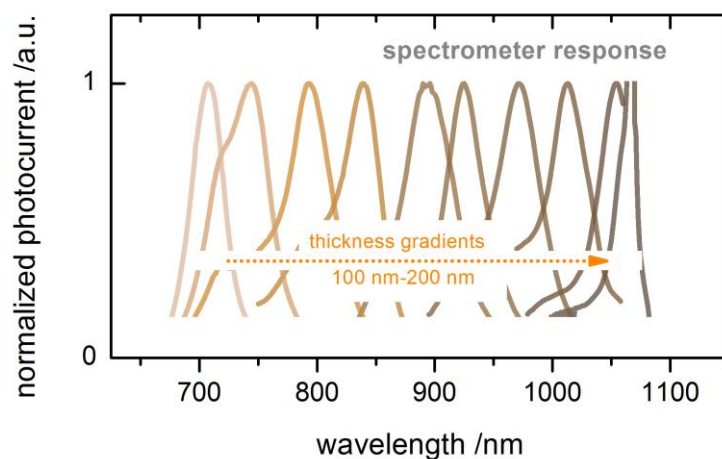


**Figure S11. Spectral response of photodetecting pixels in a miniaturized spectrometer** with a wedged blade coated active layer based on PBTTT:PCBM. The thickness variation of the active layer ranges from 100 nm to 200 nm. The spectrum of the pixel with the longest resonance wavelength is influenced by a laser peak (at 1060 nm) from the light source used for the measurement. The resonance wavelength for the last pixel is estimated to be at 1065 nm.

Table S1. Performance parameters for metal-metal detectors based on PBTTT:PCBM, at second order resonances.

Resonance wavelength /nm	$R_{sh}$ / $10^7 \Omega \text{ cm}^2$	$I_{noise}^*$ / $A \text{ cm}^{-1} \text{ Hz}^{-1/2}$	Responsivity / $A \text{ W}^{-1}$	$D^*$ / $10^{12} \text{ Jones}$	FWHM /nm
710 ( $\pm 5$ )	0.5 ( $\pm 0.1$ )	$6.2 \times 10^{-14}$	0.20 ( $\pm 0.04$ )	3.3 ( $\pm 0.6$ )	32 ( $\pm 5$ )
775 ( $\pm 5$ )	1.0 ( $\pm 0.2$ )	$4.6 \times 10^{-14}$	0.17 ( $\pm 0.03$ )	3.6 ( $\pm 0.7$ )	27 ( $\pm 5$ )
805 ( $\pm 5$ )	1.0 ( $\pm 0.2$ )	$4.6 \times 10^{-14}$	0.16 ( $\pm 0.03$ )	3.5 ( $\pm 0.6$ )	28 ( $\pm 5$ )
870 ( $\pm 5$ )	1.5 ( $\pm 0.3$ )	$3.5 \times 10^{-14}$	0.15 ( $\pm 0.03$ )	4.2 ( $\pm 0.8$ )	25 ( $\pm 5$ )
915 ( $\pm 5$ )	1.5 ( $\pm 0.3$ )	$3.5 \times 10^{-14}$	0.16 ( $\pm 0.03$ )	4.7 ( $\pm 0.9$ )	24 ( $\pm 4$ )
960 ( $\pm 5$ )	5.0 ( $\pm 0.5$ )	$1.8 \times 10^{-14}$	0.14 ( $\pm 0.05$ )	8.1 ( $\pm 2.9$ )	22 ( $\pm 4$ )

\* $I_{noise}$  is calculated for zero-voltage bias

Table S2. Performance parameters for DBR detectors based on PBTTT:PCBM, at second order resonances.

Resonance wavelength /nm	$R_{sh}$ / $\Omega \text{ cm}^2$	$I_{noise}^*$ / $A \text{ cm}^{-1} \text{ Hz}^{-1/2}$	Responsivity / $A \text{ W}^{-1}$	$D^*$ /Jones	FWHM /nm
715	$0.3 \times 10^7$	$7.4 \times 10^{-14}$	0.26	$3.5 \times 10^{12}$	19
771	$0.8 \times 10^7$	$4.4 \times 10^{-14}$	0.25	$5.7 \times 10^{12}$	15
835	$1.3 \times 10^7$	$3.5 \times 10^{-14}$	0.20	$5.7 \times 10^{12}$	15
907	$3.5 \times 10^7$	$2.2 \times 10^{-14}$	0.19	$8.6 \times 10^{12}$	14

\* $I_{noise}$  is calculated for zero-voltage bias

## References

- Hendriks, K. H., Li, W., Wienk, M. M. & Janssen, R. A. J. Small-Bandgap Semiconducting Polymers with High Near-Infrared Photoresponse. *J. Am. Chem. Soc.* **136**, 12130–12136 (2014).
- Yu, Y. *et al.* A perylene bisimide derivative with a LUMO level of  $-4.56 \text{ eV}$  for non-fullerene solar cells. *J. Mater. Chem. C* **4**, 4134–4137 (2016).
- Fourier-transform photocurrent spectroscopy of microcrystalline silicon for solar cells. *Appl. Phys. Lett.* **80**, 719–721 (2002).
- Vandewal, K. *et al.* Fourier-Transform Photocurrent Spectroscopy for a fast and highly sensitive spectral characterization of organic and hybrid solar cells. *Thin Solid Films* **516**, 7135–7138 (2008).
- Kishino, K. *et al.* Resonant cavity-enhanced (RCE) photodetectors. *IEEE J. Quantum Electron.* **27**, 2025–2034 (1991).
- Li, G. *et al.* ‘Solvent Annealing’ Effect in Polymer Solar Cells Based on Poly(3-hexylthiophene) and Methanofullerenes. *Adv. Funct. Mater.* **17**, 1636–1644 (2007).
- Miller, N. C. *et al.* Factors Governing Intercalation of Fullerenes and Other Small Molecules Between the Side Chains of Semiconducting Polymers Used in Solar Cells. *Adv. Energy Mater.* **2**, 1208–1217 (2012).
- Vandewal, K., Tvingstedt, K., Gadisa, A., Inganäs, O. & Manca, J. V. Relating the open-circuit voltage to interface molecular properties of donor:acceptor bulk heterojunction solar cells. *Phys. Rev. B* **81**, 125204 (2010).